THE ASTROPHYSICAL JOURNAL, 456:437–444, 1996 January 10

ABELL 2163: TEMPERATURE, MASS, AND HYDROSTATIC EQUILIBRIUM

M. MARKEVITCH,[1,2] R. MUSHOTZKY,[3] H. INOUE,[1] K. YAMASHITA,[4] A. FURUZAWA,[4] AND Y. TAWARA[4]

Received 1995 February 6; accepted 1995 June 26

ABSTRACT

Using *ASCA* data, we have measured the electron temperature in Abell 2163 out to 1.5 h^{-1} Mpc ($\frac{3}{4}$ of the virial radius, or $10a_X$, where a_X is the X-ray core-radius) from the center, in three radial bins. The obtained temperatures are $12.2^{+1.9}_{-1.2}$ keV, $11.5^{+2.7}_{-2.9}$ keV, and $3.8^{+1.1}_{-0.9}$ keV in the $0–3a_X$ (0–3′.5), $3–6a_X$ and $6–13a_X$ spherical shells, respectively. [Errors are 90% throughout the paper unless otherwise stated, and $h \equiv H_0$(100 km s^{-1} Mpc^{-1})$^{-1}$.] Formally applying the hydrostatic equilibrium and spherical symmetry assumptions and using these data together with the *Ginga* spectral and the *ROSAT* imaging data, we were able to severely limit the possible binding mass distribution of the generic form $\rho = \rho_0(1 + r^2/a_b^2)^{-n/2}$. All the allowed binding mass profiles are steeper than the gas density profiles, and mass profiles with the same slope as gas are excluded at a greater than 99% confidence. The total mass inside 0.5 h^{-1} Mpc is $4.3 \pm 0.5 \times 10^{14}$ h^{-1} $M_\odot$, of which $0.074h^{-3/2}$ is gas, while inside $1.5h^{-1}$ Mpc, the mass is $1.07 \pm 0.13 \times 10^{15}$ h^{-1} $M_\odot$.

The strongest constraint on the mass profile is the observed quick drop of the temperature at large radii, which can be reconciled only marginally with the *ROSAT* detection of gas at an even greater radius. We note that in the outer part of this cluster, which is likely to be a recent merger, the timescale for reaching electron-ion temperature equality via collisions is comparable to the merger timescale, so the measured electron temperature may give an underestimate of the gas pressure there. Otherwise, if our low value is indeed representative of the gas temperature in the outer shell, the cluster atmosphere should be convectionally unstable, and gas turbulence should exist. Bulk motions of the gas are also expected during the merger. Their existence would increase the total gas pressure above that indicated by the observed temperature. Thus, failure of the model in which dark matter and gas have the same distribution at the radii of interest, which is favored by hydrodynamic simulations, may be due to the neglect of these phenomena, which leads to an underestimate of the total density and an overestimate of the baryonic fraction at large radii. The mass estimate at the smaller radius, where there is no evidence of departing from equilibrium, is likely to be correct.

Our measured electron temperatures, combined with the previously reported Sunyaev-Zeldovich decrement toward this cluster and the *ROSAT* gas density profile, under the assumption of spherical symmetry, are consistent with a Hubble constant between 42 and 110 km s^{-1} Mpc^{-1} (68% interval), where the uncertainty is dominated by that of the available SZ measurement.

Subject headings: dark matter — distance scale — galaxies: clusters: individual (A2163) — X-rays: galaxies

1. INTRODUCTION

After the realization that extended X-ray emission from clusters is due to hot optically thin plasma (e.g., Mitchell et al. 1976; Mushotzky et al. 1978), it was suggested that measuring the spatial distribution and the temperature of this emission would allow a relatively robust determination of the cluster binding mass distribution (e.g., Fabricant, Rybicki, & Gorenstein 1984), provided that the gas is in hydrostatic equilibrium in the cluster gravitational well. This method requires a spatially resolved temperature measurement, which was impossible until recently. Thus, previous estimates have usually assumed that the cluster gas is isothermal, outside the sometimes cooler central regions (for the most recent application, see, e.g., Elbaz, Arnaud, & Böhringer 1995, hereafter EAB, who analyzed Abell 2163). However, *Ginga* scanning of the Coma Cluster (Hughes 1991) and recent *ROSAT* spatially resolved temperature measurements (e.g., in Abell 2256; Briel & Henry 1994) indicate that the cluster temperature structure may be complex, although approximate isothermality is indeed observed inside the central several core radii. Below, we add to these data with an *ASCA* detection of the temperature decline in the outer part of Abell 2163, whose temperature profile appears to resemble that of Coma, the only other cluster in which at the moment the gas temperature is measured out to a comparable radius. Moreover, our data imply that the gas cannot be in hydrostatic equilibrium at the observed temperatures in the outer part of this cluster, which probably underwent a recent merger (Soucail, Arnaud, & Mathez 1995; EAB). Earlier, using the gravitational lensing and X-ray data, Loeb & Mao (1994) demonstrated that in another, apparently relaxed cluster, Abell 2218, gas in the central part cannot be in pressure equilibrium at the measured temperature, and a similar problem was noted by Daines et al. (1995) in Abell 1689. These findings may indicate that more physics should be taken into account before using X-ray measurements to estimate cluster masses.

In this paper, we continue to analyze the 1993 August *ASCA* observation of Abell 2163, the hottest and most luminous of known clusters (mean T_e = 12–15 keV, EAB, our estimate; L_X[2–10 keV] = 6×10^{45} ergs s^{-1}, Arnaud et al. 1992), situ-

[1] ISAS, 3-1-1 Yoshinodai, Sagamihara, Kanagawa 229, Japan. E-mail: maxim, inoue@astro.isas.ac.jp.
[2] Permanent address: IKI, Profsoyuznaya 84/32, Moscow 117810, Russia. E-mail: maxim@hea.iki.rssi.ru.
[3] NASA/GSFC, Greenbelt, MD 20771. E-mail: mushotzky@gsfc.nasa.gov.
[4] Department of Physics, Nagoya University, Furo, Chikusa, Nagoya 461-01, Japan. E-mail: yamasita, furuzawa, tawara@phys.nagoya-u.ac.jp.

ated at $z = 0.201$ with a galaxy radial velocity dispersion of 1680 km s^{-1} (Soucail et al. 1995; Arnaud et al. 1994). It possesses the most luminous and extended radio halo of those detected so far (Herbig & Birkinshaw 1995). Some preliminary *ASCA* results, which include the detection of the H-like iron line in the cluster spectrum and the gas temperature variations in the cluster central part, are presented in Markevitch et al. (1994, hereafter Paper I). Details of the data reduction relevant to the results reported here and the obtained temperature distribution are presented below in § 2 and in the Appendix. In § 3, these new temperatures, the *ROSAT* density profile, and the Sunyaev-Zeldovich measurement by Wilbanks et al. (1994) are used to estimate the Hubble constant. In § 4, an attempt is made to constrain the cluster binding mass distribution, formally applying the hydrostatic equilibrium assumption. In § 5, we point to the possibilities of the deviation from the equilibrium.

2. MEASURING THE TEMPERATURES

Details of the observation used here are given in Paper I. Our aim now is to obtain the large-scale temperature distribution in Abell 2163. To do this, we used data from both the GIS and SIS, restricting our analysis to energies above 2.5 keV to avoid uncertainty of the excessive absorption toward this cluster (EAB) and because of the still uncertain instrument calibration at lower energies. We collected spectra in three rings of radii 0–3.5, 3.5–7.5, and 7.5–11.5 centered on the cluster brightness peak, in five energy bins, 2.5–3, 3–4, 4–5, 5–7, and 7–11 keV. They were simultaneously fitted by a model consisting of a spherically symmetric β-model gas density distribution (Jones & Forman 1984) with its parameters fixed at their *ROSAT* values ($a_X = 1.2 \pm 0.075$ and $\beta = 0.62^{+0.015}_{-0.02}$; EAB), with the constant temperatures in the corresponding spherical shells of radii 0–2.9, 2.9–6.3, and 6.3–13a_X being free parameters. We chose $13a_X$ as an outer radius in the model (which is the maximum radius at which the emission was actually detected at the 90% confidence by *ROSAT*; EAB). The exact value of this radius does not significantly affect the results. The outer radius of the third image ring is chosen smaller than that to reduce the background contribution and to exclude the uncalibrated detector areas. The *ROSAT* density profile, derived from the PSPC data (whose angular resolution is better than that of *ASCA*) in the assumption of isothermality, is adequate for this hot cluster even in the presence of significant temperature variations, since, as the plasma temperature changes from 3 to 15 keV, its emissivity in the *ROSAT* band changes by only 20%. We also show below (§ 2.2) that this density profile is consistent with the *ASCA* image. A rudimentary correction of the *ROSAT* emission measure for nonisothermality has nevertheless been made in each shell (which for the detected temperature decline roughly corresponds to an increase of β to 0.64), which had no significant effect on the results. Each layer was projected to the sky, multiplied by the telescope efficiency, convolved with the mirror PSF dependent on the energy and the focal plane position, and its contribution to each image ring was calculated for each energy, for the two GIS detectors and four SIS chips. The Raymond & Smith (1977 [1992 version]) model has been used for the model spectrum, fixing the redshift at 0.2 (Soucail et al.), the abundance at 0.4 (Paper I), and the absorption at log $N_H = 21.22$ (EAB). Details of the procedure are given in the Appendix. Figure 1 shows the data values for six detectors and three image rings, along with the best-fit model. Figure 2 shows the resulting best-fit temperatures, $12.2^{+1.9}_{-1.2}$ keV, $11.5^{+2.7}_{-2.9}$ keV, and $3.8^{+1.1}_{-0.9}$ keV in the three spherical regions, respectively (the errors are 90% confidence for one interesting parameter). The fit is good, with $\chi^2 = 69/90 - 8$ d.o.f. (eight parameters include three temperatures, a single normalization for both GISs, and four separate normalizations for the SIS chips; see below). The confidence intervals given above are obtained by Monte Carlo simulation (in 90% of the trials, the best-fit value of a temperature was within this interval) and incorporate errors of the background and the PSF model used. These two most serious sources of the potential systematic error are detailed below, before we discuss the physical implications of this measurement.

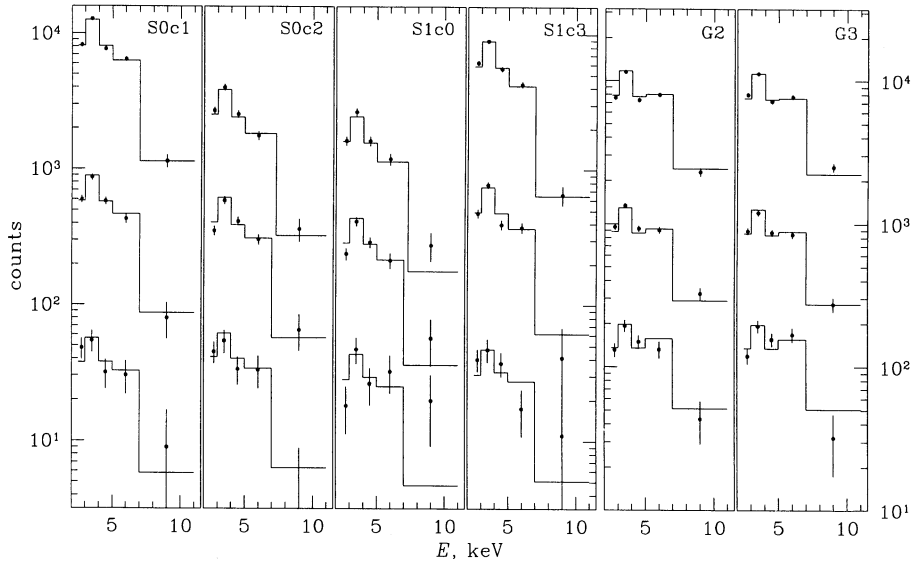

FIG. 1.—Spectra of the three image regions (in detector counts) and the best-fit model (see Fig. 2). Panels correspond to the four SIS chips and the two GISs whose data were fitted simultaneously. Upper, middle, and lower spectra correspond to central, middle, and outer image rings, respectively (values for the central region are multiplied by a factor of 2 for clarity). Plotted errors are 1 σ, including errors of the background but not including the PSF systematics.

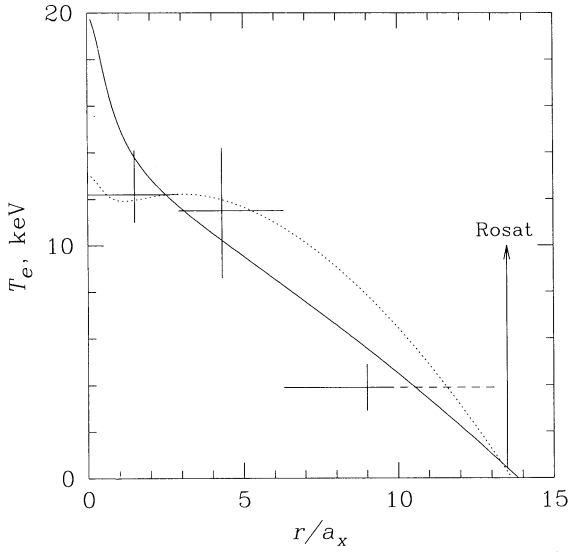

FIG. 2.—Deprojected temperatures in three spherical regions of the cluster, obtained with GIS + SIS, are shown as crosses. Vertical bars are single-parameter 90% intervals that include all known systematic errors. Crosses are centered at the EM-weighted radius for each bin. For the outer region, spectra were collected from the ring with the outer radius smaller than that used for the model, which is shown by the dashed line. The arrow corresponds to (at least) a 90% lower limit on the temperature at about $13a_X$, which arises from the *ROSAT* detection of the cluster emission at that radius. The smooth solid line shows one of the allowed temperature profiles (that for $n = 2.4$ and $a_b = 0.5a_X$) under the hydrostatic equilibrium assumption. A temperature profile for the mass model with the same a_b as above but with the slope similar to that of gas, $n = 3\beta = 1.9$, excluded at a >99% confidence, is shown as a dotted line.

2.1. *Background Subtraction*

For the temperature decline in the outer region to be an artifact, the GIS background has to be about 2 times lower than we assumed. The day-to-day 1 σ variation of the GIS background rate integrated over the detector, for the same geomagnetic rigidity value, is 20%–30% (Kubo 1994). We ensured a better accuracy (about 6%) by first reconstructing the background from a set of the blank field observations, normalized according to their exposures and the distribution of the geomagnetic cutoff rigidity during the observation, and then fitting a normalization of this model background image to the outer parts of the GIS images of our particular observation. The cluster emission scattered to the image regions used for the background fit was removed using a β-model cluster brightness convolved with the mirror PSF. Obtained normalization coefficients for both GISs were consistent with 1 (as was expected for our observation date from the monitoring by Kubo 1994). A similar method is not applicable to the SIS with its smaller field of view, and we assumed an error of 20% on the normalization of the SIS background calculated from the blank fields, analogous to that of GIS.

2.2. *Mirror PSF*

The mirror PSF has a half-power diameter of about 3′ and wide wings whose shape depends on energy and the focal plane position (Serlemitsos et al. 1995; Takahashi et al. 1995). Because of the wide PSF, the flux in the outer ring is in fact dominated by that scattered from the inner cluster part, and the fraction of the scattered flux is energy dependent. For example, for our gas density profile and a constant temperature, fractions of the flux from the inner, middle, and outer three-dimensional model shells are (0.80, 0.18, 0.02) in the inner image ring, (0.41, 0.43, 0.16) in the second ring, and (0.28, 0.24, 0.48) in the outer ring for $E = 2.5$ keV, while for $E = 10$ keV, the respective fractions are (0.79, 0.18, 0.03), (0.43, 0.41, 0.16), and (0.40, 0.24, 0.36). The inward contributions are mainly due to projection effects, and the outward contributions are because of the PSF scattering. These numbers illustrate the degree of correlation between the measured temperatures and show that even though the image rings are much larger than the PSF half-power diameter, flux from the inner cluster regions can be extremely important in the outer rings, while the inward contributions are small. One also notices that the sign of the energy dependence of these fractions is such that, if these effects are not accounted for, the outer part of an isothermal cluster would appear hotter. These effects are largest for the hotter systems with small angular scale lengths such as Abell 2163.

To take this scattering into account, we have used a two-dimensional model of the mirror PSF with 1′ resolution, obtained by interpolation between a set of high-quality narrowband GIS images of Cyg X-1, a bright point source with a hard spectrum, observed at 11 focal plane positions (Takahashi et al. 1995; Ikebe 1995). This PSF model ignores the differences among the four instruments and irregularities of each mirror and cannot be used at the energies below 2 keV. The model reproduces an actual point source radial brightness profile reasonably well, and a 1 σ systematic error of 5% on the PSF integral over concentric rings of a width of several arcminutes has been assumed. We have added this error to contributions of the inner model shells to the outer image regions during the Monte Carlo calculation of the confidence intervals (see the Appendix), conservatively assuming that the error is the same (100% correlated) in all energy bands. However, for the SIS, it may be an underestimate of the error, because neither of the image regions is contained within one chip, while the PSF uncertainties for integration regions other than concentric rings are not well understood and are larger, because of the ignored mirror asymmetries. For SIS, we used the Cyg X-1 images, smoothed to compensate for the effects of the relatively insignificant but energy-dependent intrinsic GIS resolution, and the SIS cluster images were also smoothed to the same final resolution before collecting the ring spectra.

An analog of the PSF systematic error was added to the data errors when calculating the reported best-fit χ^2 values (see the Appendix), although χ^2 is reasonable even without this correction. To confirm that our PSF model is adequate, we have attempted to free the parameters of the density profile, a_X and β, and fit them together with the temperatures in three model shells to the GIS data in the same rings as above (excluding SIS for simplicity). The resulting two-parameter confidence contours in the a_X-β plane, obtained by fitting the three temperatures for each pair of a_X and β, are presented in Figure 3 and are perfectly consistent with the *ROSAT* isothermal fit of the brightness profile. A direct comparison in the *ROSAT* energy band cannot be performed at the moment since the mirror PSF below 2 keV is unknown. We conclude that our procedure is adequate, and we are justified to fix a_X and β at their values as listed in EAB.

2.3. *SIS/GIS/Ginga Consistency*

We analyzed the SIS and GIS data separately and obtained results which are in good agreement. Using the GIS data only, the temperatures in the three regions are $11.6^{+2.2}_{-1.2}$ keV, $14.1^{+4.3}_{-3.9}$

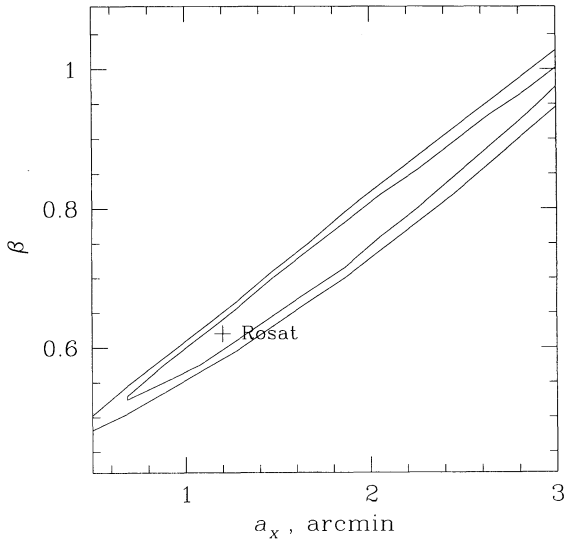

FIG. 3.—Confidence contours for the density profile parameters a_X and β, obtained by letting temperatures in the three model shells vary freely and fitting the data from the two GISs. The contours correspond to 68% ($\chi^2_{min} + 2.3$) and 90% ($\chi^2_{min} + 4.61$) joint two-parameter confidence. A cross marks the *ROSAT* best-fit values for the isothermal fit ($a_X = 1'.2$, $\beta = 0.62$). Our best-fit values are $a_X = 1'.4$, $\beta = 0.66$, and the temperatures 12.2 keV, 12.7 keV, and 3.7 keV, with $\chi^2_{min} = 21.8/30 - 6$ d.o.f.

keV, and $3.9^{+1.6}_{-0.9}$ keV, with $\chi^2 = 24.5/30 - 4$ d.o.f. Using two chips in each SIS detector (which subtend a $11' \times 22'$ rectangle in the sky, thus covering only a part of the outer ring), we obtained $12.6^{+3.5}_{-2.3}$ keV, $8.7^{+4.1}_{-2.9}$ keV, and $3.4^{+2.4}_{-1.3}$ keV, with $\chi^2 = 39.4/60 - 7$ d.o.f. (all errors are 90% confidence uncertainties). The cluster is significantly asymmetric; in order to accommodate this effect, we allowed the relative normalizations of the four chips to be free parameters. We chose to use only GIS data for the Hubble constant estimate to ensure that errors are evaluated correctly (see § 2.2) but to include SIS data in the binding mass estimate to get a better constraint on the temperature in the outer cooler region.

A *Ginga* LAC wide-aperture spectrum of Abell 2163 was analyzed in Arnaud et al. (1992) and in EAB. Fitting the *Ginga* spectrum alone in the 3–30 keV band by an isothermal model, we obtained $T_e = 13.5^{+1.8}_{-1.5}$ keV with $\chi^2 = 6.1/18 - 2$ d.o.f., fixing other parameters as above.[5] Although the *Ginga* spectrum is consistent with a single-temperature model, it allows the kind of nonisothermality observed by *ASCA*, because only about 15% of the overall cluster emissivity comes from our outer shell. A simultaneous fit of the SIS, GIS, and *Ginga* data gives the temperatures 13.3 keV, 13.3 keV, and 3.8 keV for the three model regions, with $\chi^2 = 81.3/108 - 9$ d.o.f., in which 44.7 is due to the SIS, 27.0 due to the GIS, and 9.6 due to *Ginga*. Comparing these numbers to the χ^2 values obtained in separate fits for each instrument, we conclude that there is a reasonable agreement among all instruments. We note, however, that the overall GIS best-fit temperature, 11.5 keV, is somewhat lower than the *Ginga* temperature (although they are consistent at the 95% level), which may have an effect on the mass estimate (for which we used the *ASCA* and *Ginga* data jointly) comparable with its statistical error.

Finally, we have undertaken a less model-dependent analysis of the Abell 2163 two-dimensional temperature distribution, using the actual *ROSAT* image as a model brightness distribution, and the result suggests that the projected temperatures are lower in all four directions off the center (Markevitch et al. 1995). Thus, the effect we report in this paper seems to be real, unless there remains some gross misunderstanding of the telescope systematics. Unfortunately, because of the poor statistics far from the cluster center, it is difficult to test this measurement with *ROSAT*, even though the temperatures are getting close to its 2 keV upper energy limit. Analysis of the archival *ROSAT* data in a ring from 3'.5–7'.5 gives $T_e = 15^{+\infty}_{-10}$ keV and in a ring from 7'.5–11'.5, $T_e = 4^{+32}_{-2}$ keV. Thus, these values are consistent with the *ASCA* results but with much larger uncertainties.

3. HUBBLE CONSTANT

Wilbanks et al. (1994) detected a Sunyaev-Zeldovich decrement toward Abell 2163. We have used this measurement to estimate the Hubble constant, following the method proposed by Gunn (1978), Silk & White (1978), and Cavaliere, Danese, & De Zotti (1979), and most recently applied to Abell 665 by Birkinshaw, Hughes, & Arnaud (1991), to Abell 2218 by Birkinshaw & Hughes (1994), and to Cl 0016+16 by Yamashita (1994). Wilbanks et al. presented their measurement in terms of the peak y value for their assumed isothermal symmetric gas model, $y_0 = 3.78 \pm 0.62 \times 10^{-4}$ (1σ error; a component of the error arising from uncertainties of the gas model parameters is excluded). In the absence of the original radio scans, we simulated them using the gas model of Wilbanks et al. and recalculated the normalization of the SZ profile for our temperatures and the EAB value of a_X, β, and ρ_{g0}, crudely corrected for the nonisothermality (see § 2.1). The resulting value for the Hubble constant has a best fit of 63 km s^{-1} Mpc^{-1} and a 68% confidence interval of 42–110 km s^{-1} Mpc^{-1}. The confidence interval has been calculated by Monte Carlo simulation and is dominated by the uncertainty of the currently available SZ measurement. Under the assumption of an isothermal gas extending to $r = 13a_X$ and a best-fit temperature of 14.6 keV (*Ginga* + *ROSAT* PSPC), the best-fit H_0 value is 93 km s^{-1} Mpc^{-1}.

4. BINDING MASS

Hydrodynamic simulations of the growth of clusters in a hierarchical universe (e.g., Evrard 1990; Navarro, Frenk, & White 1995) predict temperature profiles in equilibrium clusters generally similar to what we have observed, a nearly isothermal inner part in which most of the X-ray emission originates, and a decline of the temperature in the outer part. However, the predicted temperature drop in the outer regions is not as steep as we have detected. In Coma, the only other cluster thus far with the temperature measured out to the comparable off-center distance (Hughes 1991), the temperature profile is rather similar to that in Abell 2163.

We will now use our temperatures, supplemented by the *Ginga* spectrum and the *ROSAT* image, to try to constrain the cluster binding mass distribution, formally applying the assumptions of hydrostatic equilibrium and spherical symmetry, following the formalism of Hughes (1989) and Henry, Briel, & Nulsen (1993). Although below we show that for

[5] A somewhat too low value of χ^2 is due to our assumption that the *Ginga* background errors in different energy channels are uncorrelated, but since *Ginga* results are mostly superseded by the current *ASCA* measurement, we will not concentrate on that.

several reasons, hydrostatic equilibrium is an unlikely condition in the outer parts of this cluster, it is useful to obtain the mass estimate under this assumption both for comparison with previous estimates and to get an idea about the possible errors it can introduce.

The gas density is assumed to have the profile $\rho_g = \rho_{g0}(1 + r^2/a_X^2)^{-3\beta/2}$ with a_X and β fixed at their *ROSAT* values, which is adequate out to large radii (EAB). Although nonisothermality would modify this profile derived in the assumption of the constant temperature, this would have a minor effect on the conclusions. For the binding mass profile of the generic form $\rho = \rho_0(1 + r^2/a_b^2)^{-n/2}$, we tried to find the values of ρ_0, a_b and n consistent with the data. For such distributions of the gas and the binding mass, the temperature radial profile is determined by four parameters, ρ_0, a_b, n, and the central gas temperature T_0. For several n from the range of interest, a continuous temperature profile was reconstructed for each point in the (ρ_0, a_b) plane and compared to the *ASCA* + *Ginga* data set (modeling the spectra in each *ASCA* image ring and the overall spectrum for *Ginga*), fitting the remaining parameter T_0 to minimize the overall χ^2. We then crudely compared the obtained temperature profile with the *ROSAT* data (analyzed in EAB), ignoring the *ROSAT* spectral information and using only the fact that in its 0.4–2 keV band image, there is emission out to a certain radius, which implies that the temperature at that radius is above zero. Thus, for the radii in which the model temperature dropped below zero (which means that there is no gravitationally bound gas there), we calculated χ^2 with which the 1′-binned *ROSAT* radial brightness profile differs from zero. The 90% constraints in the ρ_0-a_b plane, corresponding to $\chi^2_{\rm min} + 4.61$ for *ASCA* + *Ginga* and $\chi^2 = 4.61$ for *ROSAT*, are shown in Figure 4.

Figure 4 shows that only a very small region of the parameter space is marginally allowed by both data sets, namely, the region with binding mass profiles steeper than that of the gas. Among the models allowed by *ASCA* + *Ginga*, the *ROSAT* data allow only those with $n \gtrsim 2.1$ and a_b smaller than or equal to the gas scale length. An additional restriction is that the total density cannot be below the gas density at the radii at which the gas is actually observed. For X-ray–measured quantities, $\rho/\rho_g \propto h^{3/2}$, and this condition excludes the models with $n \gtrsim 2.7$ and $n \gtrsim 3$ (among those otherwise allowed by all data) for $h = 0.5$ and $h = 0.8$, respectively—and if any amount of dark matter is to exist at all in the cluster outskirts, this restriction should be stronger. Mass profiles with the same slope as that observed for the gas, that is, $n = 3\beta$, which are favored by hydrodynamic simulations,[6] are excluded at a $> 99\%$ confidence for all a_b. A temperature profile from the allowed region for $n = 2.4$ is shown in Figure 2. The binding density and the enclosed mass profiles that correspond to this model are shown in Figure 5 (for $h = 0.5$), together with the gas mass from EAB. For the allowed models, the enclosed binding mass depends only mildly on n. Inside $r = 0.5\ h^{-1}$ Mpc the mass is $4.3 \pm 0.5 \times 10^{14}\ h^{-1}\ M_\odot$ (of which $0.074\ h^{-3/2}$ is gas), and inside $r = 1.5\ h^{-1}$ Mpc it is $1.07 \pm 0.13 \times 10^{15}\ h^{-1}\ M_\odot$ (in which the gas fraction is $0.14\ h^{-3/2}$, while the fraction of the gas density in the total mass density at this radius is as high as $0.23\ h^{-3/2}$). The quoted 90% errors correspond to the full range of mass for the models that satisfy all restrictions. The mass inside $r = 0.75\ h^{-1}$ Mpc is slightly lower but marginally consistent with the value given in EAB, $7.3 \pm 0.8 \times 10^{14}\ h^{-1}\ M_\odot$, the difference arising from the slightly different overall temperatures used. At the larger radii, our allowed masses are considerably lower (by a factor of 1.5 at $r = 15a_X$ for the

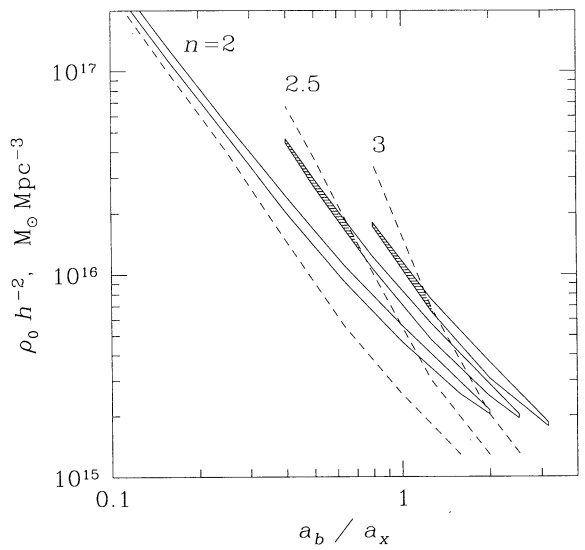

FIG. 4.—Constraints on parameters of the binding mass distribution, for three fixed values of n. Regions inside the solid contours are allowed by the *ASCA* + *Ginga* data at the 90% confidence, while the *ROSAT* imaging data, for the same value of the remaining parameter T_0, exclude the region above the dashed curve at the 90% confidence at least. The regions marginally allowed by both data sets are shaded. Models with $n \gtrsim 3$ or $n \gtrsim 2.7$ are excluded for $h = 0.8$ or $h = 0.5$, respectively, because the total density becomes lower than the observed gas density at some radii in those models.

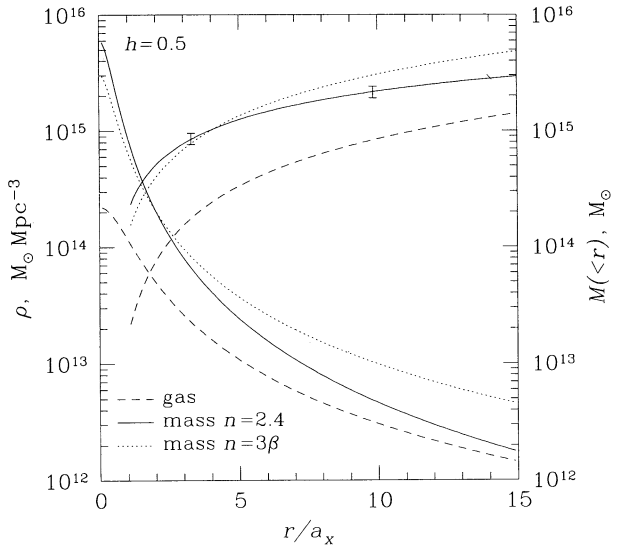

FIG. 5.—Radial profiles of the gas (from EAB) and the total mass, for $h = 0.5$. Descending lines show density, and ascending lines show enclosed mass. The solid line corresponds to the total mass model with $n = 2.4$ and $a_b = 0.5a_X$, allowed by the constraints in Fig. 4 under the hydrostatic equilibrium assumption. Error bars at $r = 3.3a_X$ and $9.8a_X$ correspond to the 90% confidence intervals on the total mass, calculated for the models complying with all constraints. However, hydrostatic equilibrium is likely to be broken in the cluster's outer part; see § 5.2. The dotted line corresponds to one of the excluded models in which the mass profile has the same slope as that of gas.

[6] Simulations by, e.g., Evrard (1990) and Navarro et al. (1995) predict the slope of the dark matter profile to be only slightly steeper than that of the gas for the regions outside cores in equilibrium clusters.

enclosed mass) than the estimate given in EAB obtained assuming isothermality. However, below (§ 5.2) we will show that in the outer part, the gas hydrostatic equilibrium assumption may be invalid, and we are likely to underestimate the mass at the larger radius.

5. DISCUSSION

5.1. *The Overall Temperature*

The high value of the cluster overall temperature obtained by *Ginga* and *ASCA* is in line with the cluster's high X-ray luminosity and its velocity dispersion (Arnaud et al. 1992; Soucail et al. 1995; Lubin & Bahcall 1993; however, its velocity dispersion may be overestimated because of the substructure). This temperature is not affected by the presence of the diffuse radio halo or the existence of a possible AGN in the cluster.

Herbig & Birkinshaw (1995) discovered a radio halo in this cluster, the most luminous and extensive halo of those detected, and estimated that as much as 10% of the cluster's X-ray emission in the 0.5–4.5 keV band may be produced by the inverse-Compton scattering of cosmic microwave background photons by the relativistic electrons of the halo. If the relativistic electrons have the power-law energy distribution over a range of energies and if the halo has the typical steep radio spectrum (so that its X-ray photon index is $\alpha_{\text{X-ray}} = \alpha_{\text{radio}} \approx 2.2$, e.g., Jaffe 1977; see review in Sarazin 1988), an inverse-Compton contribution to the cluster X-ray spectrum is expected to be between 4% and 7% over the energy band 5–20 keV; therefore, the temperature measurement should be essentially unaffected. When we limit the flux of the power law component to less than 7% of the total flux in our energy band and let its index vary, the best-fit temperature in the inner shell (using GIS) is $10.6^{+1.8}_{-1.9}$ keV at 68% confidence, consistent with the model without a power-law component. If we fix the index at a value of 2.2, the upper limit on the power-law contribution to the total flux in our band is 3.5% (90% confidence).

The possibility of a significant AGN contribution to the cluster X-ray spectrum was considered by Arnaud et al. (1992), who included a nonthermal component with the AGN spectrum in their fit to the *Ginga* data in the 2–20 keV energy band, and concluded that such a component should be negligible. From a spectral fitting point of view, the possibility of an additional AGN component is similar to that of the diffuse component considered above and results in similar upper limits. Furthermore, a detection of the H-like iron Kα line in the *ASCA* SIS cluster spectrum (Paper I) confirms that the gas is indeed very hot—the H-like to He-like iron line ratio limits the temperature of the gas that emits iron lines to at least 12 keV, assuming ionization equilibrium.

5.2. *The Mass Distribution*

The analysis presented in § 4, made under the hydrostatic equilibrium assumption, may be interpreted as showing that the binding mass distribution is well restricted out to the large off-center distances, and most interestingly, one can rule out a distribution of dark matter similar to that of the baryonic gas. However, it can be seen from Figure 2, which also shows one of the excluded temperature profiles from the family of models in which mass has the same slope as gas, that it is excluded mainly because the observed temperature is too low in our outer radial bin, while *ROSAT* detects emission at a greater radius. Although, as is shown in § 4, there is still room for some of the more exotic total mass distributions (which assume even more exotic dark matter profiles), we note that there are at least a few natural reasons for the observed temperature to be lower than that predicted by an equilibrium model. The observed steep temperature drop between the middle and the outer radial shells implies that they are convectionally unstable because the equivalent polytropic index is ~ 1.9. Even if convection is slow and local pressure equilibrium is always achieved, the measured temperature in the outer cluster part would give an underestimate of the total pressure, since bulk motions of the gas would account for some fraction of it.

One also notes that although Abell 2163 does not exhibit the prominent substructure that is observed in many other clusters, it may still have recently undergone (or be undergoing) a merger, as suggested by Soucail et al. (1995) from the galaxy velocities, by EAB from the morphology of the *ROSAT* image, and in Paper I from the small-scale nonisothermalities near the cluster center. Simulations suggest (e.g., Navarro et al. 1995) that a high value of $\beta_T \equiv \mu m_p \sigma^2_{\text{gal}}/kT$, which is 1.3–1.5 for this cluster (from the data in the references above), is also a property of nonrelaxed clusters. If the merger is still going on, the gas outside the cluster's hot central region may not have settled down and is continuing to inflow with the bulk velocities as high as 1000–2000 km s^{-1}, as some merger simulations predict (see, e.g., Fig. 3*e* in Schindler & Müller 1993). If such flows exist, the gas kinetic energy can be as high as $\mu m_p \sigma^2_{\text{gas}}/2 \sim 3$–5 keV per particle, comparable with its thermal energy, making the hydrostatic equilibrium assumption invalid in the outer cooler region. The measured temperature would then again lead to an underestimate of the total pressure at those distances.

Another possible result of a recent merger is absence of electron-ion equipartition. At the distance of $10a_X$ in Abell 2163, the electron density is about $10^{-4}\, h^{1/2}$ cm^{-3} (EAB), and the timescale for reaching electron-ion temperature equality via collisions is $1\text{–}2 \times 10^9\, h^{-1/2}$ yr (Spitzer 1956), comparable to the merger timescale. Thus, for the gas heated by shock waves during a merger, the measured electron temperature would give an underestimate of the gas pressure at those distances shortly after the merger. Note that for electron densities and temperatures in the range of interest, the characteristic time of change of the ion fractions for highly ionized iron is about an order of magnitude shorter than the above timescale (e.g., Mewe & Gronenschild 1981); therefore, the emission in the iron spectral lines should be consistent (at least with the present experiment accuracy) with the electron temperature and will not indicate that electrons and ions are out of equipartition. The SZ effect (Sunyaev & Zeldovich 1972) is proportional to the electron temperature and will not show it, either. Figure 2 shows that an underestimate of the thermodynamic temperature in our outer shell by a factor of $\gtrsim 2$ could produce the observed discrepancy with the model in which dark mass has a distribution similar to that of gas (and could also result in the conclusion about convectional instability). The mass profile that corresponds to this excluded model (Fig. 5, *dotted lines*) illustrates that such an underestimate of the outer temperature would have little effect on our total mass estimate at the smaller radius, while the mass within $r = 10a_X$ may be significantly underestimated.

The discovery of the strongest radio halo in this hottest cluster may have another implication relevant to our discussion. All radio halos are found in hotter clusters, and it is

not ruled out that the energy spectrum of the halo's relativistic electrons extends to low enough energies to efficiently heat the intracluster gas (Lea & Holman 1978; Vestrand 1982; Sarazin 1988 has a discussion), with the heating rate that may even exceed the X-ray radiation cooling. If such heating is indeed present, the gas in the inner region may have insufficient time to equalize its increasing pressure with the outer shells. Such a regime would require a net energy supply over the region occupied by the halo (1.2 h^{-1} Mpc; Herbig & Birkinshaw 1995), about an order of magnitude higher than the cluster X-ray luminosity. Since there is no apparent way to test it observationally, we only mention that it may lead to an overestimate of the binding mass in the cluster's inner part. A weak extended magnetic field whose presence is indicated by the radio halo should have an energy density negligible compared to the gas pressure and therefore will not affect the mass determination on the large linear scale.

To conclude, although we did not explore the effects of the cluster asymmetry and possibly more complex temperature structure in detail (such a study in now under way), the observed discrepancy between the data and the simple model in which dark matter and gas have similar distributions most naturally indicates that some of the gas equilibrium assumptions do not hold in the outer part of this cluster.

6. SUMMARY

We have performed a spatially resolved temperature measurement of Abell 2163, the hottest cluster known, and have found that it is cooler beyond 1 h^{-1} Mpc from the center, similar to Coma and to the hydrodynamic simulation predictions. Combining our temperature measurements with the *ROSAT* imaging and the *Ginga* wide-aperture spectrum, we were able to severely restrict the possible binding mass distributions of the form $\rho = \rho_0(1 + r^2/a_b^2)^{-n/2}$, if not exclude them all, formally applying the assumption that the gas is in hydrostatic equilibrium at the measured temperatures. However, this assumption is likely to be inadequate in this nonrelaxed cluster at large off-center distances, where, for example, convection should exist because of the steep temperature drop, or bulk gas motions are expected during a merger, or the electron-ion temperature equipartition timescale becomes comparable to the merger timescale. If true, this would lead to a significant underestimate of the gravitating mass density in the cluster outskirts, which would lead to large apparent values of the baryonic density. We have also estimated H_0 using the *ASCA* electron temperatures and the previously reported *ROSAT* density profile and the Sunyaev-Zeldovich decrement. The obtained value is poorly constrained, however, because of the large uncertainty of the available SZ measurement.

We are grateful to all members of the *ASCA* team for the continuous support. We thank A. C. Fabian for interesting discussions and the referee for many useful suggestions. M. M. would like to thank ISAS for its support and hospitality during this work.

APPENDIX A

MODELING THE TELESCOPE RESPONSE WITH WIDE PSF

As we mentioned in § 2.2, the wide energy- and position-dependent *ASCA* mirror PSF requires that the spectra from different image regions be fitted simultaneously. To do this within a reasonable computing time, we have used the following simple scheme. Denoting the projected sky image of the emission measure of the ith model region (either two- or three-dimensional) as m_i; its spectrum normalized to the unit emission measure as $s_i(E)$ (where E is in keV); the total number of the model regions as M; the operation of summing the flux over the jth detector image region as R_j (including in it the SIS gaps and the GIS grid for clarity); the spectrum from the jth detector image region as $d_j(E')$ (where E' is in channels); the total number of the detector image regions as N; the linear operation of multiplying by the mirror effective area plus PSF scattering, which converts a model brightness distribution into that in the detector plane, as $P(E)$; and convolution of the spectrum with the coordinate-independent detector spectral response including the detector efficiency, which converts kilo–electron volts to channels, as D, we have

$$d_j = DR_j \sum_{i=1,M} Pm_i s_i \, .$$

The telescope response transform, $T_{ij}(E) \equiv R_j \sum_{i=1,M} P(E)m_i$, which for a given energy converts the spectra of the model regions to the fluxes in the detector image regions, $d = DTs$, is thus an $M \times N$ matrix that includes geometry of the source and the integration regions, vignetting, and PSF scattering. The least-squares solution s is searched by iterations among the desired model spectra. If there is no PSF scattering and no projection, T is diagonal, and spectra from the different image regions can be fitted separately. If m_i can be fixed or reasonably simply parameterized (for example, a *ROSAT* image is available or a β-model brightness profile can be assumed), $T(E)$ can be calculated once in the beginning (which involves time-consuming two-dimensional convolutions with the position-dependent PSF), after which only the spectral parameters and perhaps relative normalizations of the model spectra need to be fitted, each iteration involving only the convolution with the small matrix T (for reasonable M and N). In the fit of our three temperatures assuming a fixed β-model emission measure profile, T was a 3×3 matrix for each energy. To fit the density profile parameters in addition to the temperatures, we have calculated the transform for the 16 1′ wide radial model shells (that is, T was a 16×3 matrix), assuming uniform emission measure throughout the cluster, and only recalculated the normalization for each shell in each iteration according to the values of a_X and β, taking advantage of linearity of all the involved operations.

The telescope PSF is poorly known at the moment, and an estimate of its systematic error has been included in the analysis. We assumed a 5% 1 σ error (Takahashi et al. 1995; see § 2.2) of the nondiagonal elements of the matrix T. In Monte Carlo calculation of the confidence intervals of the model temperatures (§ 2), a 5% random error has been added directly to the elements of T. For calculation of all the $\chi^2_{\min}$ values and confidence contours presented in the paper, an approximate equivalent of this error, σ_j, has

been added in quadrature to the statistical error of the data value d_j:

$$\sigma_j^2 = \sum_{i \neq j} \left(0.05 d_i \frac{T_{ij}}{T_{ii}} \right)^2$$

(which is a slight overestimate because of the neglect of nondiagonal elements of T). Here T is a matrix calculated for the adequate emission measure distribution and the model regions that are the same as the data regions. If the data rings are narrower than, say, 3′–4′, an error should be added to the diagonal elements of T as well.

The code which implements this scheme can be obtained by anonymous ftp from hea.iki.rssi.ru, file pub/maxim/soft/asca_clust.tar.gz.

REFERENCES

Arnaud, M., Elbaz, D., Böhringer, H., Soucail, G., & Mathez, G. 1994, in New Horizon of X-Ray Astronomy, ed. F. Makino & T. Ohashi (Tokyo: Universal Academy), 537
Arnaud, M., Hughes, J. P., Forman, W., Jones, C., Lachieze-Rey, M., Yamashita, K., & Hatsukade, I. 1992, ApJ, 390, 345
Birkinshaw, M., & Hughes, J. P. 1994, ApJ, 420, 33
Birkinshaw, M., Hughes, J. P., & Arnaud, K. A. 1991, ApJ, 379, 466
Briel, U. G., & Henry, P. 1994, Nature, 372, 439
Cavaliere, A., Danese, L., & De Zotti, G. 1979, A&A, 75, 322
Daines, S., Jones, C., Forman, W., & Tyson, A. 1995, ApJ, submitted
Elbaz, D., Arnaud, M., & Böhringer, H. 1995, A&A, 293, 337 (EAB)
Evrard, A. E. 1990, ApJ, 363, 349
Fabricant, D., Rybicki, G., & Gorenstein, P. 1984, ApJ, 286, 186
Gunn, J.E. 1978, in Observational Cosmology, ed. A. Maeder et al. (Sauverny: Geneva Observatory), 1
Henry, J. P., Briel, U. G., & Nulsen, P. E. J. 1993, A&A, 271, 413
Herbig, T., & Birkinshaw, M. 1995, BAAS, 26, 1403
Hughes, J. 1989, ApJ, 337, 21
———. 1991, private communication, presented in Clusters and Superclusters of Galaxies, ed. A. C. Fabian (Dordrecht: Kluwer), 54
Ikebe, Y. 1995, Ph.D. thesis, Tokyo Univ.
Jaffe, W. J. 1977, ApJ, 212, 1
Jones, C., & Forman, W. 1984, ApJ, 276, 38
Kubo, H. 1994, private communication
Lea, S. M., & Holman, G. D. 1978, ApJ, 222, 29
Loeb, A., & Mao, S. 1994, ApJ, 435, L109
Lubin, L. M., & Bahcall, N. A. 1993, ApJ, 415, L17
Markevitch, M., et al. 1995, in preparation
Markevitch, M., Yamashita, K., Furuzawa, A., & Tawara, Y. 1994, ApJ, 436, L71 (Paper I)
Mewe, R., & Gronenschild, E. H. B. M. 1981, A&AS, 45, 11
Mitchell, R., Culhane, J., Davison, P., & Ives, J. 1976, MNRAS, 189, 329
Mushotzky, R. F., Serlemitsos, P. J., Smith, B. W., Boldt, E. A., & Holt, S. S. 1978, ApJ, 225, 21
Navarro, J. F., Frenk, C. S., & White, S. D. M. 1995, MNRAS, in press
Raymond, J. C., & Smith, B. W. 1977, ApJS, 35, 419
Sarazin, C. L. 1988, X-Ray Emission from Clusters of Galaxies (Cambridge: Cambridge Univ. Press)
Schindler, S., & Müller, E. 1993, A&A, 272, 137
Serlemitsos, P., et al. 1995, in preparation
Silk, J. I., & White, S. D. M. 1978, ApJ, 226, L103
Soucail, G., Arnaud, M., & Mathez, G. 1995, in preparation
Spitzer, L., Jr. 1956, Physics of Fully Ionized Gases (New York: Interscience)
Sunyaev, R. A., & Zeldovich, Ya. B. 1972, Comments Astrophys. Space Phys., 4, 173
Takahashi, T., Markevitch, M., Fukazawa, Y., Ikebe, Y., Ishisaki, Y., Kikuchi, K., Makishima, K., & Tawara, Y. 1995, *ASCA* Newsletter, No. 3 (NASA/GSFC)
Vestrand, W. T. 1982, AJ, 87, 1266
Wilbanks, T. M., Ade, P. A. R., Fischer, M. L., Holzapfel, W. L., & Lange, A. E. 1994, ApJ, 427, L72
Yamashita, K. 1994, in New Horizon of X-Ray Astronomy, ed. F. Makino & T. Ohashi (Tokyo: Universal Academy), 279